Ultra-Compact CMOS-Compatible Ytterbium Microlaser

Zhan Su,[1] Jonathan D. B. Bradley,[1,2] Nanxi Li,[1,3] E. Salih Magden,[1] Purnawirman,[1] Daniel Coleman,[4] Nicholas M. Fahrenkopf,[4] Christopher Baiocco,[4] Thomas N. Adam,[4] Gerald Leake,[4] Douglas D. Coolbaugh,[4] Diedrik Vermeulen,[1] and Michael R. Watts[1,*]

[1]*Research Laboratory of Electronics, Massachusetts Institute of Technology, 77 Massachusetts Avenue, Cambridge, MA 02139, USA*
[2]*Current address: Department of Engineering Physics, McMaster University, 1280 Main Street West, Hamilton, ON L8S 4L7, Canada*
[3]*John A. Paulson School of Engineering and Applied Sciences, Harvard University, 29 Oxford Street, Cambridge, MA 02138, USA*
[4]*Colleges of Nanoscale Science and Engineering, State University of New York Polytechnic Institute, 257 Fuller Road, Albany, NY 12203, USA*
mwatts@mit.edu

Abstract: We demonstrate a waveguide-coupled trench-based ytterbium microlaser, achieving a sub-milliwatt lasing threshold and a 1.9% slope efficiency within an ultra-compact 40-μm-radius cavity while maintaining full compatibility with a CMOS foundry process.

OCIS codes: (130.3120) Integrated optics devices; (230.5750) Resonators; (140.0140) Lasers and laser optics.

1. Introduction

The CMOS-compatibility of silicon photonics enables low-form-factor and low-cost integrated optical circuits. Due to these advantages silicon photonics is having a large impact on transceiver technology and new applications such as optical interconnects [1,2], sensors [3,4] and quantum computation [5] are on the horizon. The combination of biomedical sciences with silicon photonics offers compact and packaged devices at a low cost for sensing applications where large equipment was previously required. In order to achieve high-sensitivity detection of small biological particles, both passive high-quality factor (Q-factor) cavities [6] and active laser cavities [7] have been extensively investigated. Active laser cavities are generally preferred for their narrow linewidths. Previously, microtoroid [7] or microsphere [8] laser cavities have been demonstrated as promising platforms for bio-sensing applications. However, such microcavity configurations require external optical fibers for pump power input and laser output coupling, which limits their CMOS compatibility and integration within silicon photonic systems.

Trench-based microlasers co-integrated with silicon nitride waveguides (Fig. 1 (a)) can resolve the incompatibility and provide a mechanically stabilized system. The bus waveguide is fabricated near the trench-based cavity for both pump power input and laser output. The coupling area is naturally isolated from the cavity with SiO_2 cladding and the cavity is, by itself, a reservoir to hold and interact with nanoparticles. Reducing the size of the cavity while maintaining lasing behavior will not only enable denser integration using state-of-art foundry processes but also improve the detection sensitivity [7]. While lasing behaviors in trench-based cavities have been demonstrated in a wide range of wavelengths using different rare-earth-ions (Yb^{3+}, Er^{3+}, Tm^{3+} etc.) [9,10], the size limit of the design remains relatively unexplored.

Here, we provide a detailed analysis of the trench-based microcavities with different sizes and demonstrate lasing behaviors with ytterbium ion doping down to 40-μm radius devices with a sub-milliwatt lasing threshold (720 μW) and a 1.9% slope efficiency. Based on the model provided in this paper, the laser size can be further reduced through using high-index host materials (TiO_2 [11], TeO_2 [12] etc.), making it possible to achieve high-density and large-scale integration at the same time.

2. Design and Experimental Results

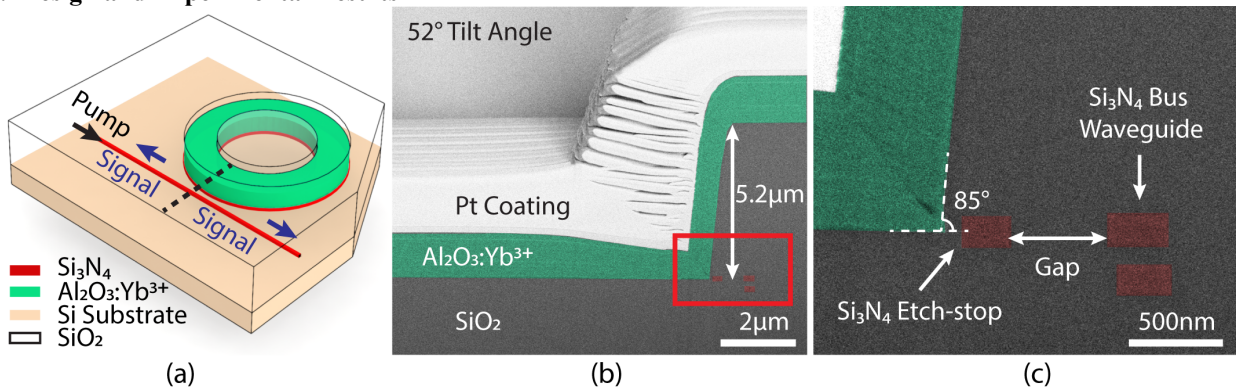

Fig. 1 – (a) Schematic of the ytterbium microlaser. (b) Cross-sectional scanning-electron-micrograph (SEM) image along the dotted line in Fig. 1(a) with an imaging tilt angle of 52º, showing a trench depth of 5.2 μm and a trench slope of 85º. Platinum coating is used during focused-ion-beam (FIB) etching to protect the cross-sectional profile. (c) Zoom-in view of the red box region in Fig. 1(b), showing Si_3N_4 bus waveguide and Si_3N_4 etch-stop layer.

The microcavities were fabricated on a 300-mm silicon wafer using 193-nm optical immersion lithography and

process steps similar to those described in [10]. A schematic of the ytterbium microlaser is shown in Fig. 1 (a). It consists of a Si_3N_4 bus waveguide and SiO_2 trench filled with ytterbium-doped aluminum oxide (Al_2O_3:Yb^{3+}). We deposited a 1600-nm-thick Al_2O_3:Yb^{3+} layer with an Yb doping concentration of 5×10^{20} cm^{-3}. The bus waveguide is used for both pump light input into and laser signal output from the cavity. Lasing behaviors can be observed on both sides of the bus waveguide due to the degeneracy of clockwise (CW) and counter-clockwise (CCW) laser modes.

To obtain an accurate profile of the resulting microcavity structure, we first deposited a protection layer of platinum (Pt) on the laser sample and then cut it along the dotted black line indicated in Fig. 1 (a) using focused-ion-beam (FIB). The resulting cross-sectional scanning-electron-micrograph (SEM) image of the microcavity is shown in Fig. 1 (b). The trench has a depth of 5.2 μm and a trench angle of ~85º. The image was taken with sample tilt of 52º with respect to horizontal plane. Taking this into account, the ratio between the Al_2O_3:Yb^{3+} film thickness on the side wall and the total deposited film thickness (measured away from the edge of the trench) is calculated to be 0.44. A zoom-in view of the area enclosed in the red box in Fig. 1 (b) is shown in Fig. 1 (c). The bus waveguide is composed of two Si_3N_4 waveguides with ~ 350-nm width to match to the resonant mode inside the microlaser cavity for the pump wavelength. The top Si_3N_4 layer is used as both the waveguide material for the bus waveguide and etch-stop layer for the deep trench. A small Si_3N_4 piece (~ 250 nm) is observed near the SiO_2 trench as a result of the deep trench etching process.

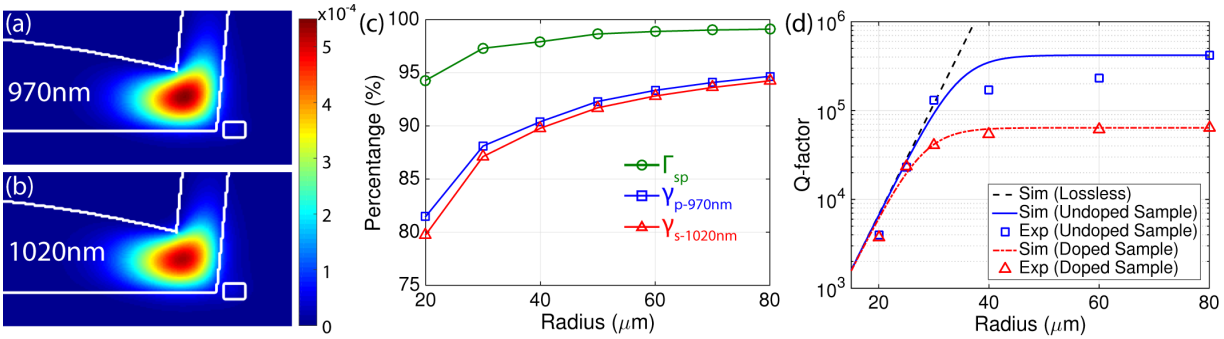

Fig. 2 – Intensity profiles of resonant modes of the microcavity laser at (a) 970 nm and (b) 1020 nm for 40-μm radius. (c) Confinement factors and intensity overlap between pump and laser mode for radii from 20 to 80 μm. (d) Microcavity Q-factors for radii from 20 to 80 μm for a wavelength of ~ 970 nm.

The fundamental resonant modes of a 40-μm radius for both pump (970 nm) and signal (1020 nm) wavelengths are shown in Fig. 2 (a) and (b). The modes are confined by the trench wall and have similar shape, indicating a large intensity overlap between pump and signal modes. To characterize the properties of the modes, we use the same definitions of intensity confinement factor ($\gamma_{s/p}$) and intensity overlap (Γ_{sp}) as in [13]. Fig. 2 (c) shows both the confinement factors ($\gamma_{s/p}$) and intensity overlap (Γ_{sp}) of the pump and signal modes. Since the resonant modes are mostly confined in the Al_2O_3:Yb^{3+} layer, the confinement factors are generally very high. Besides, the signal and pump modes are both confined by the trench wall and have similar mode profiles, making it easier to achieve high intensity-overlap between them. Therefore, with sufficiently high Q-factor, lasing can be achieved easily within the microcavity.

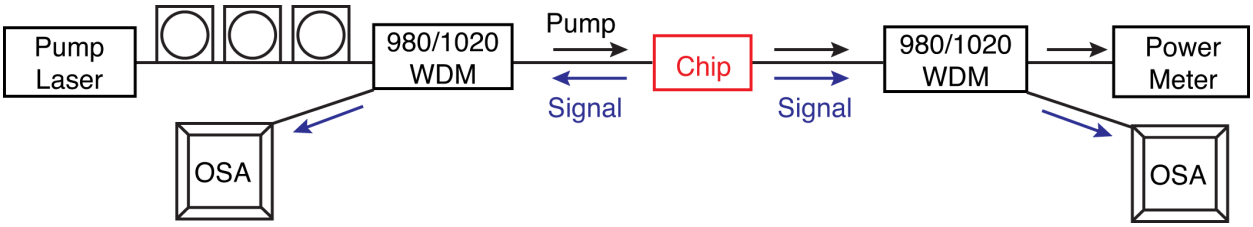

Fig. 3 – Experimental setup for measuring the Yb microlaser.

To analyze Q-factor dependence on microcavity radius, we fabricated microcavities with different radii (20, 25, 30, 40, 60, and 80 μm). Calculated and experimentally measured Q-factors for both doped and undoped microcavities are shown in Fig. 2 (d). If only radiation loss is included in the model (black dashed line), a 40-μm radius device can offer an intrinsic Q-factor on the order of 1×10^6. However, due to Al_2O_3 material loss and fabrication-induced loss, the intrinsic Q-factor of the undoped cavity is limited to 4×10^5. The difference between simulation model (solid blue line) and experiment data (square points) for the undoped sample is due to radius-related loss as a result of the trench wall and material roughness. For the doped sample, the intrinsic Q-factor of the cavity is reduced to 6×10^4 due to Yb^{3+} absorption. The experimental data matches well with the simulation because the material loss of Al_2O_3 and the trench wall and material roughness related loss are much smaller than the absorption loss of the dopants.

The experimental setup for measuring the Yb microlaser is shown in Fig. 3. A tunable pump laser is coupled onto the chip via a tapered fiber. The polarization of the pump laser is adjusted by a three-paddle polarization

controller. The laser signals are then coupled off the chip and collected by the optical spectrum analyzers (OSAs) on both sides of the chip following 980/1020 nm wavelength division multiplexers (WDMs) to separate pump and signal light. The residual pump light is coupled into a power meter for microcavity resonance identification.

The tunable pump laser used in the experiment has a maximum output power of ~3.5mW. Lasing is observed for devices with a radius $\geq$ 40 μm, where the intrinsic loss of the cavity is relatively small compared to the pump absorption loss due to Yb^{3+} ions, which translates into a net gain at signal wavelengths. The laser output spectra of the 40-μm radius microcavities with different gap sizes are shown in Fig. 4 (a) with a pump wavelength ~ 972 nm. Multimode lasing behaviors are observed for devices with 400, 500, and 600-nm gap sizes. The on-chip laser power versus on-chip pump is displayed in Fig. 4 (b). A lasing threshold of 720 μW (600-nm gap) and double-side slope efficiency of 1.9% (400-nm gap) are demonstrated.

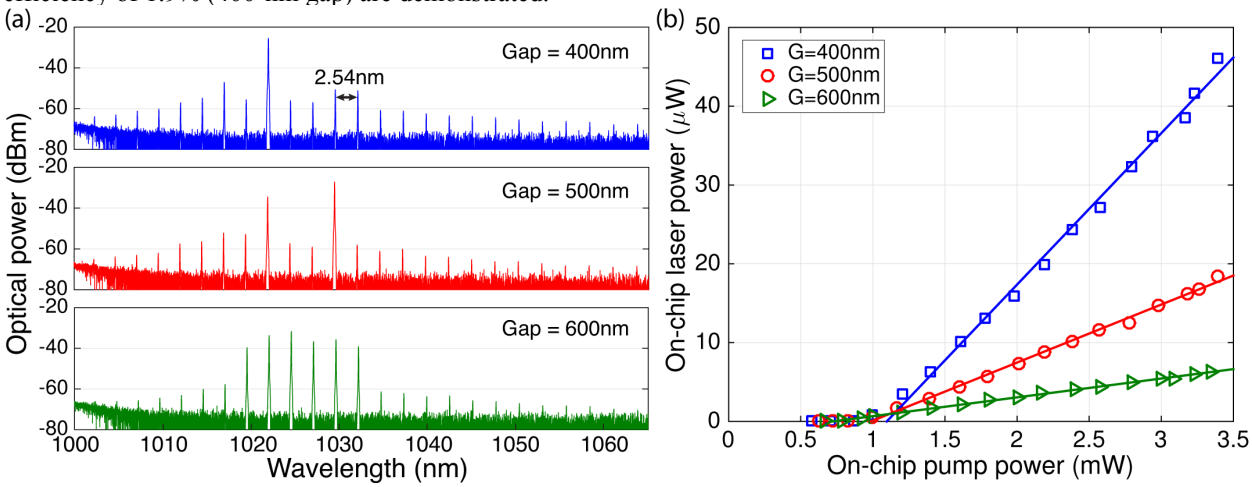

Fig. 4 – (a) Spectrum of the output laser for gap sizes of 400, 500 and 600nm. (b) On-chip laser power versus on-chip pump power for gap sizes of 400, 500 and 600nm.

While the microlaser demonstrated in this paper has a minimum radius of 40 μm, high-index materials such as titanium dioxide (TiO_2) and tellurium dioxide (TeO_2) as the host materials for rare-earth-ions can potentially allow higher intrinsic Q-factor at smaller radius and therefore achieve lasing with even more compact cavity sizes using the same trench-based microcavity. While other microcavity lasers have limited compatibility with a CMOS process, trench-based microlasers provide seamless integration with readily available silicon photonic device libraries such as high-speed detectors, modulators and full integration with state-of-art CMOS driving circuits, making it a viable method for future lab-on-chip biosensing applications.

3. Conclusion

We have demonstrated a CMOS-compatible 40-μm radius trench-based ytterbium laser on a silicon chip. The laser shows a slope efficiency of ~1.9% and a sub-milliwatt threshold. Its silicon compatibility and compact size make it possible to integrate such lasers within advanced silicon systems.

This work was supported by the Defense Advanced Research Projects Agency (DARPA) Microsystems Technology Office's (MTO) DODOS program, grant no. HR0011-15-C-0056. N. Li acknowledges a fellowship from the Agency of Science, Technology and Research (A*STAR), Singapore.

4. References

[1] E. Timurdogan, *et al.*, "An Ultra Low Power 3D Integrated Intra-Chip Silicon Electronic-Photonic Link," in Optical Fiber Communication Conference Post Deadline Papers, OSA Technical Digest (online) (Optical Society of America, 2015), paper Th5B.8.
[2] K. T. Settaluri, *et al.*, "Demonstration of an Optical Chip-to-Chip Link in a 3D Integrated Electronic-Photonic Platform," European Solid-State Circuits Conference, Gratz, Austria, 4 pages, September 2015.
[3] M. Soltani, *et al.*, "Nanophotonic trapping for precise manipulation of biomolecular arrays," Nat. Nanotech. **9**, 448 (2014).
[4] A. H. J. Yang, *et al.*, "Optical manipulation of nanoparticles and biomolecules in sub-wavelength slot waveguides," Nature **457**, 71 (2008).
[5] J. L. O'Brien, *et al.*, "Photonic quantum technologies," Nat. Photon. **3**, 687 (2009).
[6] S. C. Masmanidis, *et al.*, "Multifunctional Nanomechanical Systems via Tunably Coupled Piezoelectric Actuation," Science **317**, 780 (2007).
[7] L. He, *et al.*, "Detecting single viruses and nanoparticles using whispering gallery microlasers," Nat. Nanotech. **6**, 428 (2011).
[8] J. Ward, *et al.*, "WGM microresonators: sensing, lasing and fundamental optics with microspheres," Laser Photon. Rev. **5**, 553 (2011).
[9] J. D. B. Bradley, *et al.*, "1.8-μm thulium microlasers integrated on silicon," Proc. SPIE 9744, Optical Components and Materials XIII, 97440U (February 24, 2016).
[10] J. D. B. Bradley, *et al.*, "Monolithic erbium-and ytterbium-doped microring lasers on silicon chips", Opt. Express **22**, 12226 (2014).
[11] J. D. B. Bradley, *et al.*, "Submicrometer-wide amorphous and polycrystalline anatase TiO_2 waveguides for microphotonic devices," Opt. Express **20**, 23821 (2012).
[12] S. J. Madden, *et al.*, "Very low loss reactively ion etched Tellurium Dioxide planar rib waveguides for linear and non-linear optics," Opt. Express **17**, 17645 (2009).
[13] Purnawirman, *et al.*, "C- and L-band erbium-doped waveguide lasers with wafer-scale silicon nitride cavities," Opt. Lett. **38**, 1760 (2013).